Journal of Electronic Materials (2025) 54:3760–3772
https://doi.org/10.1007/s11664-025-11836-4

ORIGINAL RESEARCH ARTICLE

Modeling and Characterization of Hybrid Thermo-Piezoelectric Cantilevers

Etienne Herth[1] · **Bruno Cavalliers**[2] · **Sarra Salhi**[1,3] · **Faten Kardous**[3] · **Dame Fall**[2] · **Lionel Rousseau**[4] · **Laurie Valbin**[4] · **Franck Lardet-Vieudrin**[2]

Received: 12 November 2024 / Accepted: 10 February 2025 / Published online: 13 March 2025

Abstract

This work investigates the design and performance of hybrid thermo-piezoelectric cantilevers (HTPCs) that enable combined piezoelectric and thermal actuation. Using COMSOL Multiphysics for multiphysics simulations and FreeFem++ for full thermo-piezoelectric coupling, we investigated the dynamic responses of HTPCs under different actuation conditions. The study focused on understanding the influence of material properties, especially Young's modulus of aluminum nitride, on the resonant frequencies and displacement characteristics. Experimental validations with a laser Doppler vibrometer confirmed the simulation results and showed minimal frequency shifts in piezoelectric actuation and significant shifts in thermal modes. The results indicate that HTPCs hold promise for use in energy harvesting and microactuation systems.

Graphical Abstract

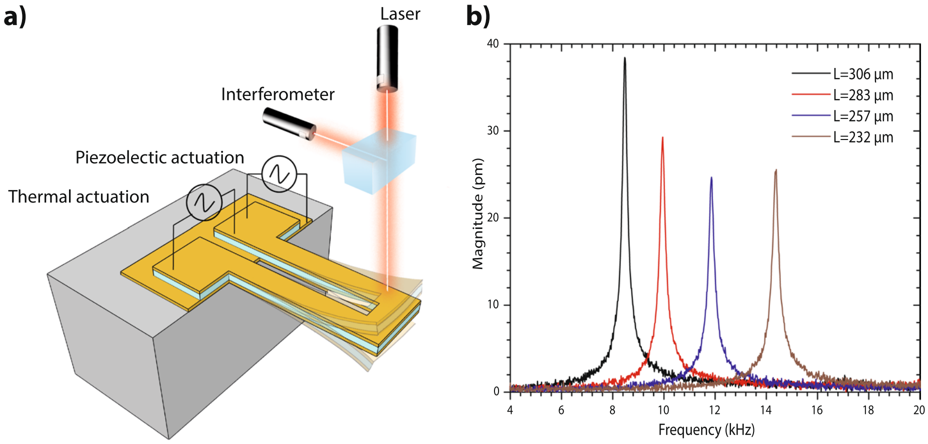

Keywords Aluminum nitride · piezoelectric actuator · thermal actuator

---

✉ Etienne Herth
etienne.herth@cnrs.fr

[1] Centre de Nanosciences et de Nanotechnologies, CNRS UMR 9001, Université Paris-Saclay, Orsay, France

[2] FEMTO-ST, Université de Franche Comté, UBFC, CNRS UMR 6174, 25044 Besançon cedex, France

[3] University of Carthage, National School of Advanced Sciences and Technologies of Borj Cedria (ENSTAB), LR16ES08 Research Laboratory of Smart Grids and Nanotechnology (LaRINa), 1164 Hammam-Chott, Tunisia

[4] University Paris Est-ESIEE-MLV, 93162 Noisy le Grand Cedex, France

Introduction

Current mainstream technology uses piezoelectric material from bulk[1–3] to thin-film layers.[4,5] Bulk piezo device fabrication is employed in both common and high-end products.[6–9] Thin-film piezoelectric materials such as zinc oxide (ZnO),[10–13] lead zirconate titanate (PZT),[14–16] and aluminum nitride (AlN)[4] are gaining increasing influence due to their favorable properties, high performance, and cointegration requirements. For the purpose of actuation, micro-devices are divided into four categories according to motion mechanisms: electromagnetic, electrostatic, piezoelectric, and thermal expansion. Electrothermal and piezoelectric actuators are the most valued because of their interesting characteristics. Piezoelectric actuators based on AlN remain a good alternative for microactuators.[17,18] This biocompatible material is characterized by a wide bandgap (6.0–6.1 eV),[19,20] high thermal conductivity (319 W/m K),[21] and low thermo-optical coefficient (2.7×10^{-5} K^{-1}),[22] which makes it suitable for applications in medicine and optics from ultraviolet (UV) to mid-infrared (IR).[23,24] Thermal actuators, on the other hand, can produce high displacements and large forces based on a cost-effective process.[25–27] Although the applied voltages for thermal actuation have been reduced, their motion performance remains to be improved. Rakotondrabe et al.[28] fabricated a thermo-piezoelectric microactuator based on the thermal bimorph principle and PZT piezo cantilever microactuation. The application of an electrical field led to initial bending of the cantilever, while varying the temperature led to a secondary bending due to the difference in the thermal expansion between layers.[29] Pourrostami et al.[30] presented an analytical model for a hybrid thermo-piezoelectric microactuator with a double-PZT cantilever beam structure consisting of two arms with different lengths. However, the combination of both types of motion actuation, piezoelectric and thermal, is still not well understood. Indeed, the design strategy should consider a number of aspects in addition to the type of actuation, such as the choice of material, geometric design, processability, and mechanical performance for a specific application. Therefore, it is difficult to develop a general research methodology and studies for each micro-device.

Numerous studies have explored various geometries and excitation mechanisms of cantilevers, including piezoelectric, thermal, and hybrid actuators. Much of this research was motivated by applications in atomic force microscopy (AFM) in the 1990s. However, these early studies focused primarily on fundamental principles and were often limited to specific applications, such as mode splitting due to clamping effects or excitation by Schottky barriers.[31,32] Despite these fundamental investigations, the combined effects of thermal and piezoelectric actuation, especially in unconventional geometries such as U-shaped hybrid thermo-piezoelectric cantilevers (HTPCs), remain insufficiently studied.

Our work deals with the investigation of the interaction of these actuation mechanisms, taking into account the influence of material properties, component geometry, boundary conditions, and fabrication imperfections. Herein, we present a methodology to characterize the performance of the HTPC that combines experimental validation with numerical modeling. This approach not only deepens our understanding of hybrid actuator technology, but also demonstrates how such devices can be used for practical applications, such as the extraction of the elastic modulus of thin films through simplified processes. The insights gained extend beyond the basic principles and provide engineers with actionable strategies to optimize the performance of microactuators for various applications.

Design and Fabrication

Chips (2×2 cm^2) of silicon-based cantilevers (so-called single-clamped beams) have been designed. As shown in Fig. 1a, we consider U-shaped HTPC of 50 µm in width (W_a), with a slit (W_b) of 10 µm width at the tip of the cantilever. As illustrated in Fig. 1b, to optimize the U-shaped HTPC design with respect to the stability of the resonant frequency and vibratory motion, we fabricated different lengths of the cantilever (L). Figure 2 shows the fabricated chip of the U-shaped HTPC, with different lengths ranging from 232 µm to 306 µm. As shown in Fig. 1, the top and bottom electrodes were sputtered from titanium and platinum layers (Ti/Pt) with a thickness of 10/100 nm in a physical vapor deposition (PVD) system (Plassys MP 500). In this work, our designed cantilever was based on TiPt/AlN/TiPt stacked layers, which were fabricated on a 500-± 25-µm-thick, 4-inch, <100>-oriented undoped silicon wafer (Si). Three UV photolithography processes were performed. The first and third processes were for metal layer deposition, and the second process was used to deposit the 1-µm-thick AlN layer using a PVD sputtering machine. Wet etching of the AlN thin film deposited by sputtering was preferred due to the very low etch rate achieved by dry etching processes.[1,33–35] As presented in Table I, both tetramethylammonium hydroxide (TMAH) and phosphoric acid (H_3PO_4) exhibit high AlN etch rates, which are particularly favorable for efficient material removal. These etch rates are considered interesting because they allow faster processing times compared to other methods while maintaining low anisotropy ratios. For the patterning of AlN, we selected an H_3PO_4 etching solution at 120 °C as it offers high selectivity against Si and ensures that the underlying silicon substrate remains

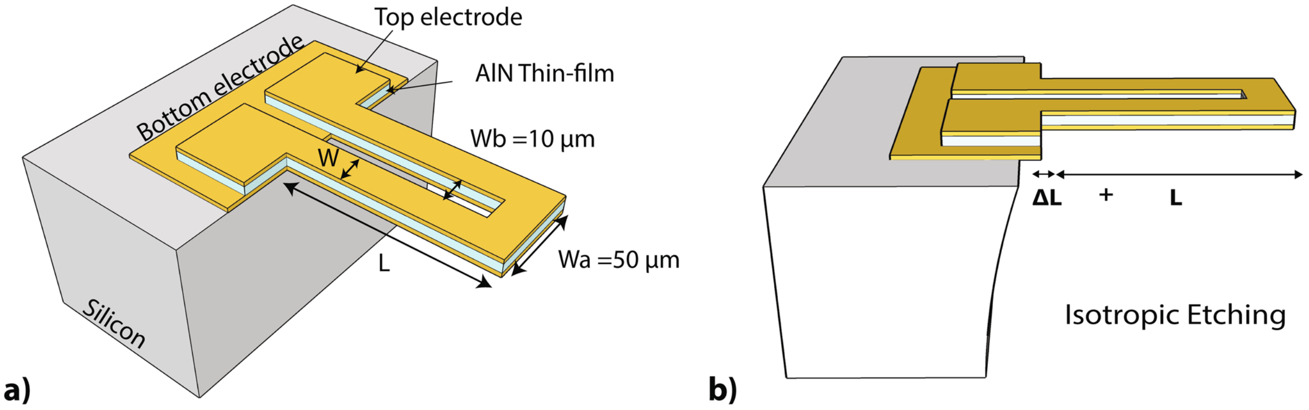

Fig. 1 (a) 3D schematic and notation of the studied U-shaped beam based cantilever, and (b) closeup of the piezoelectric stack showing the undercut released by isotropic etching.

Table I Summary of different wet chemical etching parameters of AlN using Cr as a metallic mask layer (data from Ref. 1)

Etchant	Temperature (°C)	Etching rate (nm/min)	Anisotropy ratio $R_A = t_{AlN}/u^a_{AlN}$
BHF (buffered hydrofluoric acid)	21	<0.3	1433
Al etching[b]	55	<1	412
Al etching	95	5	137
H_3PO_4 (85%)	120	20	13
TMAH (25%)	21	24	43

[a] Where t_{AlN} is the thickness of the AlN layer and u_{AlN} is the undercut distance of AlN under the etch mask

[b] A composition of phosphoric acid (80%), acetic acid (16%), and nitric acid (4%)

unaffected during the etching process. Then, the pattern of Ti/Pt/AlN was transferred directly to the silicon wafer, facilitating etch openings for the sacrificial layer. The U-shaped HTPC was released by isotropic etching of Si using pure SF_6,[36,37] as shown in Fig. 1b, and was investigated by scanning electron microscopy (SEM), as shown in Fig. 2.

Modeling

In this study, we used COMSOL and FreeFem++ for the HTPCs, which offers several advantages due to the complementary strengths of these software tools. COMSOL Multiphysics provides an extensive library of materials and their properties that can be used directly in the simulations, saving time and ensuring accuracy. The FreeFem++ software allows us to implement custom finite element formulations and solve a wide range of partial differential equations (PDEs) to enable the implementation of complex boundary conditions. To investigate and predict the behavior of the HTPC with respect to a hybrid actuation, we performed 3D finite element analysis (FEA) modeling using COMSOL Multiphysics version 5.6. As shown in Table II, the

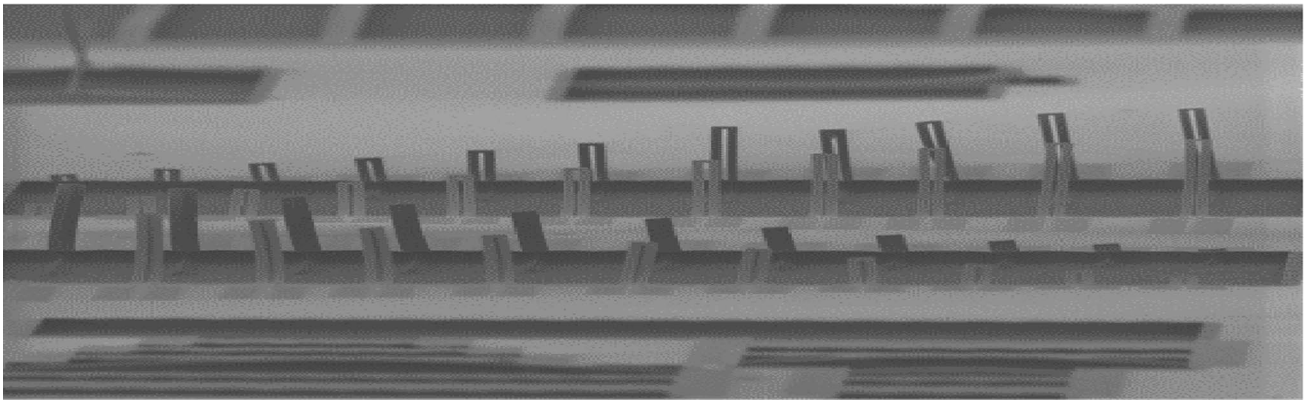

Fig. 2 Scanning electron micrograph of a released U-shaped hybrid thermo-piezoelectric cantilevers (HTPCs).

Table II Materials properties

Material	Young's modulus (GPa)	Poisson's ratio	Thermal conductivity (W/m K)
Ti	115.7	0.321	21.9
Pt	168	0.38	71.6
AlN	186	0.28	200
Si	160	0.220	34

geometry and materials used in the simulations were identical to those described for the investigated cantilever structure. The piezoelectric effect was modeled with a layered shell approach, while the thermal effect was modeled by the heat transfer in the shell. The assumed properties of AlN are given in Table III. For the mechanical boundary conditions, the silicon block was fixed at its side and base surfaces while the other faces were free to move, so that the bending effect could be obtained at a certain excitation. Different electrical boundary conditions were applied depending on the desired type of actuation. For thermal actuation, the electric field was applied between the upper HTPC electrodes, and for piezoelectric actuation, it was applied to the upper HTPC electrode while the bottom electrode was set to ground.

Here, we first simulated the two actuation modes, piezoelectric and thermal, separately and then in the hybrid mode. The main idea was to compare the simulation with experimental results to achieve a better understanding of the hybrid actuation. To improve the prediction of the resonant frequency of the device and to obtain the vibration characteristics, we also investigated the sensitivity of the model to material constants (see Table II) and to the specifics of micromachining, i.e., to the undercut caused by isotropic etching (see Fig. 1b). The effect of changing the cantilever length was also investigated for design optimization. For this purpose, the beam length was parameterized. In Fig. 3, we show the mesh of the 306-µm-long U-shaped cantilever. The meshes were created with the Gmsh finite element mesh generator.[38] The 3D mesh takes into account the prestressed state by modeling the strong initial large deformations on FreeFem++ software. These initial deformations were easily recognizable on the scanning electron micrograph (SEM), as seen in Fig. 2

Results

The HTPC was designed with three different integrated actuation on-chip configurations: piezoelectric actuation, thermal actuation, and the combination of both actuations. As shown in Fig. 4a, a laser beam was focused on the selected scan area to measure the out-off-plane resonant frequency of the cantilevers using a Polytec MSA 500 laser Doppler vibrometer (LDV),[39–41] at room temperature and atmospheric pressure.

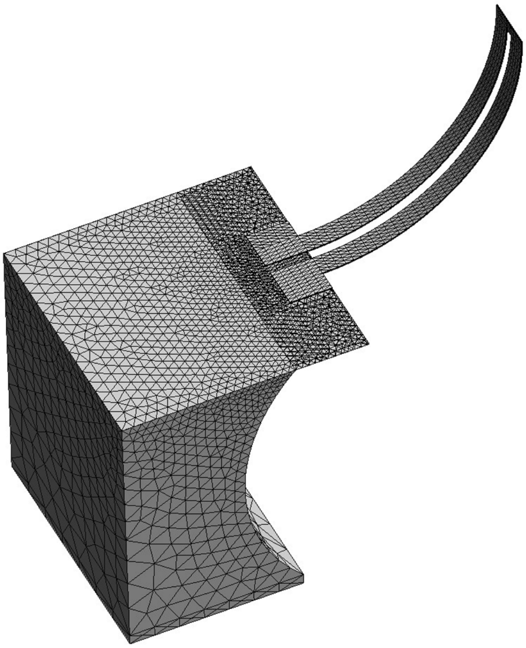

Fig. 3 Mesh of the simulated 306-µm-long cantilever at the fundamental mode.

Piezoelectric Actuation

Piezoelectric actuation was performed by applying a voltage supply between the upper and lower electrodes of the U-shaped cantilever to produce motion. We measured the resonant frequency of the fundamental mode. As shown in Fig. 4b, we found that the dynamic range was large and the resonant frequency of the fundamental mode decreased as the length of the U-shaped HTPC increased, in agreement with the analytical approximation, as follows:[18,42]

$$f_0 = \frac{1}{2\pi}\sqrt{\frac{6EI}{m_{\mathrm{eff}}L^3}} \tag{1}$$

where m_{eff}, I, L and E are the effective mass, area moment of inertia, length of the cantilever, and Young's modulus, respectively. Here, the resonance peaks present magnitude in the displacement range of 25–39 pm at 500 mV. Thus, this linear detection as a function of length allows us to accurately capture any nonlinear effects of the cantilever. This is the reason for using the piezo cantilever as a mass sensor, since the resonant frequency shifts due to the change in mass in the dynamic mode method.[43,44] As shown in Fig. 5a, for the 306-µm-long cantilever, we varied the applied voltage

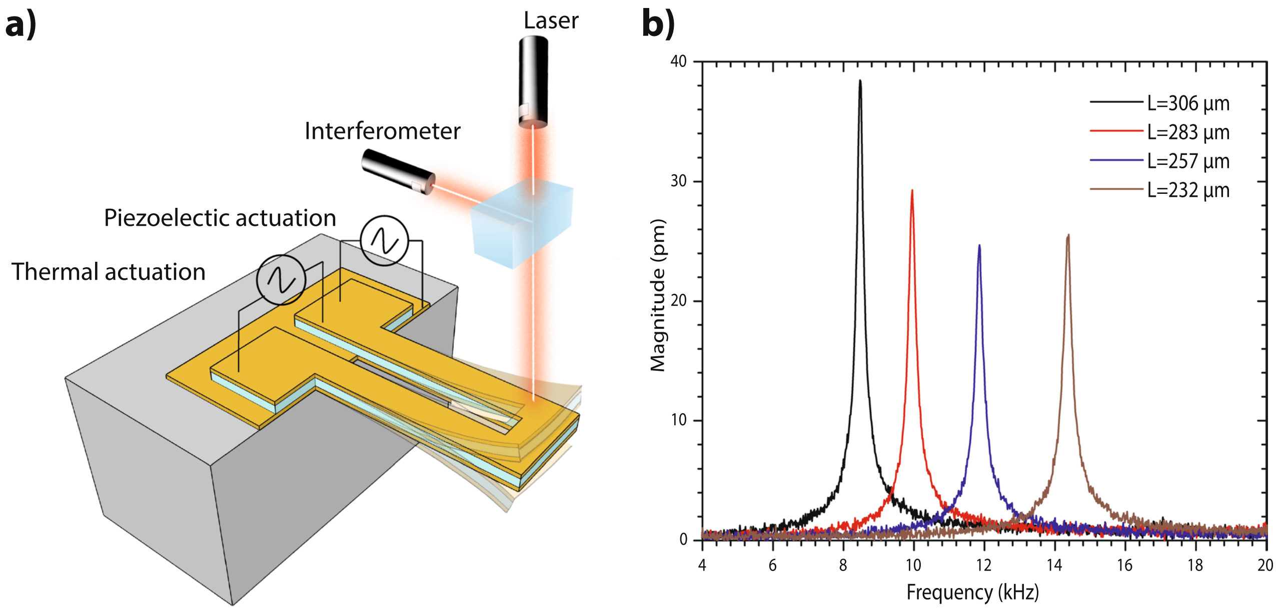

Fig. 4 (a) Hybrid thermo-piezoelectric cantilever resonance characterization setup, and (b) laser Doppler vibrometer resonance measurement of the fundamental mode for different HTPC lengths under piezoelectric actuation at 500 mV.

Table III Properties of AlN

Coefficients	Symbols	Values
Density (kg m^{-3})	ρ	3300
Compliance matrix components (10^{-12}m^{2}N^{-1})	S_{11}, S_{12}, S_{13}, S_{33}, S_{44}, S_{66}	2.8987, −0.9326, −0.50038, 2.8253, 8, 7.6628
Piezoelectric coupling coefficients (pC N^{-1})	d_{31}, d_{33}, d_{15}	−1.9159, 4.9597,−3.84
Free dielectric constants	ϵ^T_{11}, ϵ^T_{33}	9.2081, 10.1192

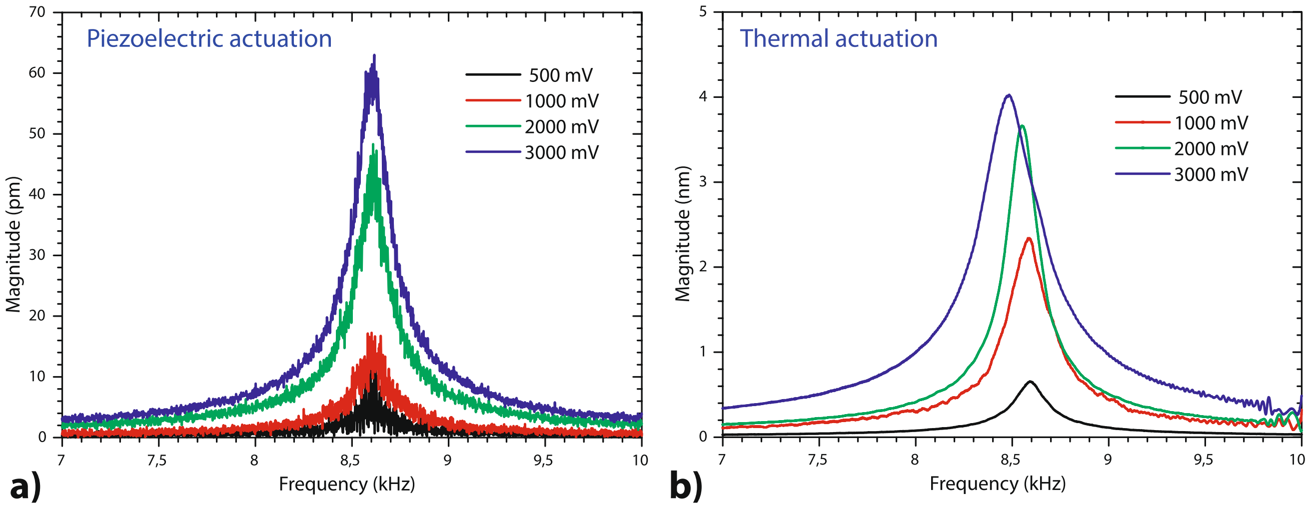

Fig. 5 Resonance measurement of the fundamental mode as a function of the applied voltage for a 283-µm-long cantilever: (a) piezoelectric actuation, and (b) thermal actuation.

in the range of 500 mV to 3 V. No shift in the resonant frequency (f_0 = 8.6 kHz) was observed regardless of the applied voltage. In the context of practical applications, the stability of the resonant frequency as a function of temperature is very important. In the next section, we investigate the motion of the U-shaped HTPCs excited by a thermal actuation configuration.

Thermal Actuation

As shown in Fig. 4a, the motion of the cantilever can also be obtained by thermal expansion caused by the current flowing through the Ti/Pt contacts of the top electrodes. We can observe in Fig. 2 that cantilevers without polarization naturally bend upward after release due to the thermal stress and the residual stress of each thin film layer. This room-temperature built-in stress σ_i resulting from the thin-film deposition process. To this stress is added a thermal stress σ_T resulting from heating caused by the applied voltage. Here, the bending effect is caused by the different thermal expansion coefficients (TEC) of the stacked layers (TiPt/AlN/TiPt). Indeed, the TEC of the AlN layer α_{AlN} (K^{-1}) is in range of $[4.3 \times 10^{-6}, 4.6 \times 10^{-6}]$, according to a study by Andrei et al.,[45] while titanium and platinum have $\alpha_{Ti} = 8.6 \times 10^{-6}\mathrm{K}^{-1}$ and $\alpha_{\mathrm{Pt}} = 8.8 \times 10^{-6}\mathrm{K}^{-1}$, respectively. The applied voltage induces a temperature increase of ΔT, reflecting the electrothermal heating of the HTPC. As a result, the cantilever expands by a length increase of δ_L as presented in Eq. 2:

$$\delta_L = \alpha_{\mathrm{AlN}} L \Delta T \tag{2}$$

where $\Delta T = T - T_0$ is the heating temperature, and T and T_0 represent the temperature of the structure in the polarized and non-polarized states, respectively. This thermally induced expansion leads to the thermal stress as follows:

$$\sigma_T = \frac{\delta_L E}{L} = \alpha_{\mathrm{AlN}} E \Delta T \tag{3}$$

Hence, the total stress is expressed as follows:

$$\sigma = \sigma_i + \sigma_T = \sigma_i - \alpha_{\mathrm{AlN}} E \Delta T \tag{4}$$

In addition to the increase in vibration magnitude thanks to the thermal actuation, the resonant frequency can also be tuned. Indeed, the initial resonant frequency (at zero heating power) was measured as the reference point. As expected, in Fig. 5b, due to the TEC of the AlN thin films, we observed an increase in the U-shaped HTPC displacement depending on the applied voltage, which varied in the range of 500 mV to 3 V. Compared to piezoelectric actuators, thermal actuators are characterized by a much higher range of motion. With increasing temperature ($\Delta\ T$), we observed a cantilever deflection described by the following equation:[25,46]

$$r = \frac{(h_t + h_b)\left[3(1+a)^2 + (1+ab)\left(a^2 + \frac{1}{ab}\right)\right]}{6(\alpha_t - \alpha_b)\Delta T(1+a)^2}, \tag{5}$$

where r is the radius of curvature of the cantilever, α_t, α_b are the TEC of the thin film test sample and base material, respectively, E_t, E_b are Young's modulus of the thin film test sample and base material, respectively, and h_t, h_b are the thickness of the thin film test sample and base material, respectively; $a = h_b/h_t, b = E_b/E_t$.

In addition to the highlighted increase in displacement, we can also observe in Fig. 5b a decrease in resonant frequency with applied voltage from 8.6 kHz (at 0.5 V) to 8.5 kHz (at 3 V). This frequency shift (Δf = 100 Hz) does not exclude an additional influence of the temperature dependence of the thermal stress ($\sigma_T = \alpha E \Delta T$) and the temperature-dependent variation in Young's modulus (E). The latter can be described by an exponential relationship of the form $E(T) = E_0 \cdot \exp(-T_0/T)$, where E_0 is Young's modulus at a reference temperature. This relationship accounts for the decrease in material stiffness with increasing temperature, which can influence the resonant frequency over the whole temperature range studied.[47] However, the exact prediction of the radius of curvature r and Young's modulus E as a function of the increase in temperature $\Delta\ T$, as approximated by Eq. 5, is not easy, mainly due to fabrication imperfections.

Model Versus Design—Sensitivity Analysis

In order to develop a reliable microsystem and offer a standard means of production from an industrialization perspective, the design must take into account the appropriate properties of the materials used to both theoretically predict and simulate their performance before fabrication and subsequent characterization. However, micro-devices are manufactured in different ways. Equation 1 highlights the importance of accurate knowledge of Young's modulus of the material. Moreover, the undercut ($\Delta\ L$) that occurred during sacrificial layer etching (see Fig. 1b) causes an increase in the cantilever length compared to the design, and thus leads to inaccurate natural frequency prediction (Eq. 1). This effective length ($L_{\mathrm{eff}} = L + \Delta L$) and the anchor modification indeed cause a deviation of the resonant frequency. Although the properties of AlN thin films are well known, herein we show that manufacturing imperfections and driving excitation must be carefully considered. As a result, device performance depends on scaling and pre- and post-manufacturing processes.

As shown in Fig. 6, to determine the real Young's modulus, simulations were carried out calculating the fundamental resonant frequency (f_0) by determining the L_{eff} for which E of the AlN film was equal and that resonated at the same frequency. We obtained a value of E close to 186

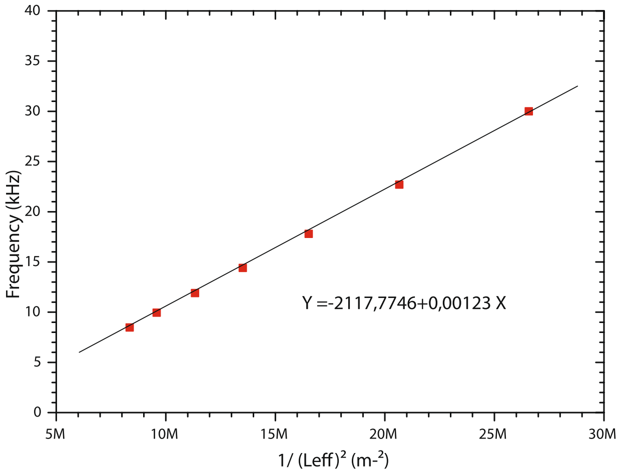

Fig. 6 Resonant frequency of cantilever at 500 mV as a function of $1/L_{\mathrm{eff}}^2$. The red line represents the regression, and its equation is given here, where Y is the resonant frequency and X is $1/L_{\mathrm{eff}}^2$.

GPa, which is quite similar to the values found in the literature between 200 GPa and 350 GPa. The experimentally measured Young's modulus of 186 GPa is lower than the bulk value of 350 GPa. This reduction is consistent with variations introduced by the deposition technique, which can result in microstructural imperfections such as porosity, grain boundary effects, or stress gradients in the thin film. These factors are well known to influence the mechanical properties of thin films relative to their bulk counterparts. Consequently, by using thermal actuation, we show that for the accurate extraction of E, the matched supply voltage (no drift effect) and manufacturing errors (e.g., underetching[37]) must be taken into account. Considering a HTPC model that accounts for the expected E and realization of imperfections, the predicted resonant frequencies are calculated for the different lengths considered. As can be seen in Table IV, the prediction agrees with the measurements, with an average error of 2.74%.

As shown in Fig. 4, the measured resonant frequency of the HTPC based on AlN thin film (E = 186 GPa) were compared with predicted shapes determined by finite element model (FEM) simulation. As presented in Table IV, we obtained a good agreement between experiments and simulation.

Table IV Comparison of measurement and simulation results

Length (µm)	F_{meas} (kHz)	F_{sim} (kHz)	Error (%)
306	8.5	8.644	1.69
283	10	9.671	3.83
257	11.8	12.085	2.42
232	14.4	13.966	3.01

Piezoelectric Combined with Thermal Actuation

The range of motion obtained using piezoelectric actuation was very limited (~ pm) (Fig. 5a), even though it was fast and precise compared with thermal actuation (~nm) (Fig. 5b). An intuitive approach for increasing the displacement amplitude was to apply a higher supply voltage. However, this is not appropriate as it can lead to depolarization of the AlN thin film and cause electrode detachment. The goal of combining the two actuation principles is to take advantage of both, namely the range of movement of thermal activation and the precision and speed of piezoelectric activation. Therefore, an effort to predict the dynamics of the combination of piezoelectric and thermal actuator simultaneously may attract attention, as this actuator can be used for a variety of applications, including energy harvesting, micro-grippers, and actuators.[27–29]

Figure 7 shows the effect of the combined piezoelectric and thermal actuators. The displacement magnitudes (~ nm) were similar to those obtained with thermal actuation only. Here, the configuration of applied voltages resulted in complex dynamic behavior. We observed drift phenomena (Fig. 7) that resulted in a shift in the resonant frequency in the range of 7.18 kHz (at 0.1 V) to 7.38 kHz (at 2 V), while it remained stable at 8.5 kHz under piezo-actuation. The shift in resonant frequency arises from the combined influence of thermal stress, induced by temperature changes, and the piezoelectric stress, resulting from the applied voltage. The thermal stress modifies the intrinsic stiffness of the cantilever by altering the mechanical properties of the material, such as the Young's modulus and stress state, through thermal expansion effects. Meanwhile, the piezoelectric effect introduces an additional strain component that

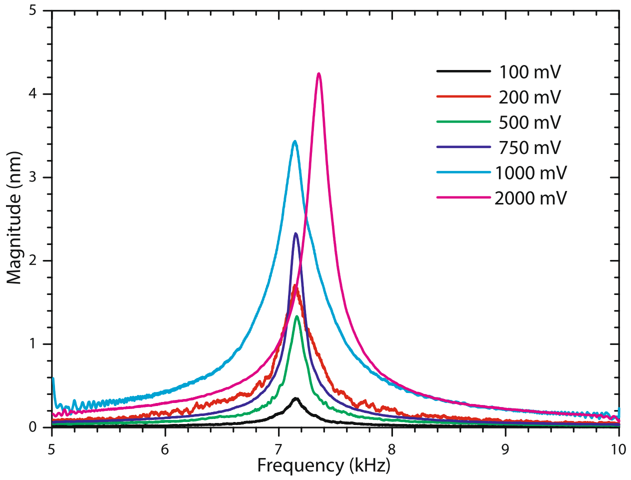

Fig. 7 Resonance measurement of the fundamental mode with different magnitude deflection as a function of the applied voltage for 306-µm-long cantilevers.

further influences the stiffness. Together, these phenomena dynamically tune the cantilever's frequency. This dual-mode actuation capability demonstrates voltage tunability, a highly desirable property for applications that require precise frequency modulation, such as sensors or resonators. Furthermore, the results highlight the potential of HTPCs for adaptive systems, where combined actuation mechanisms allow for improved functionality and versatility. To validate this behavior, the properties of the HTPCs were characterized under different activation conditions and a special test setup was developed. The results confirm that thermal activation of the U-shaped cantilever in combination with piezoelectric high-voltage excitation opens up new possibilities for advanced frequency tuning applications.[48,49] The properties of HTPCs were determined and a characterization setup was developed. The result showed that the thermal activation of the U-shaped cantilever followed by an applied high voltage and the inherent undercut allowed a mechanical resonant frequency drift and caused a potential error in the elastic modulus evaluation. Further studies could be conducted to evaluate the deflection control and further develop the thermo-piezoelectric cantilever for advanced applications. In the next section, we used the flexibility of FreeFem++ to implement customized models and boundary conditions.

Discussion

Combining piezoelectric and thermal actuation in numerical simulations was challenging because the physical and computational requirements of such piezoelectric and thermal effects are inherently coupled in certain materials, i.e., mechanical deformation, electric field, and temperature changes influence each other in complicated ways. The accurate capture of these interactions requires sophisticated multiphysics models. The coupling between thermal and piezoelectric effects often leads to nonlinear behavior, which complicates the formulation and solution of the governing equations. In addition, both the thermal and piezoelectric properties of materials can vary with temperature, which requires detailed material data and increases the complexity of the simulations. Piezoelectric materials are often anisotropic, i.e., their properties vary with direction, and this anisotropy must be accurately represented in combination with thermal effects. Applying realistic boundary conditions that reflect the actual physical scenarios can be difficult, especially when both thermal and electrical aspects are considered simultaneously. This theoretical study aimed to understand the frequency shift of the fundamental vibration mode. To this end, we used the fully coupled 3D thermo-piezoelectric finite-element model with the classical Biot (CL), Green–Lindsay (GL), and Lord–Schulman (LS) theories described in previous works[50–53] for the U-shaped beam-based cantilever.

Initially, we hypothesized the presence of a thermoelastic damping phenomenon and implemented the corresponding CL, GL, and LS finite element models.

However, according to Guha and Singh,[54,55] the maximum relative frequency shift for our aspect ratio (and the structure without voids) does not exceed 0.1%. In contrast, our thermal release model exhibited a frequency shift of about 100 Hz, which corresponds to about 1.2%. This indicates that thermoelastic damping is not the predominant process in this experimental setup. Consequently, our HTPC does not fulfill the conditions for thermoelastic damping typically modeled by GL or LS theories. Finite element simulations confirm this result, as we could not observe any significant frequency shift that could be attributed to thermoelastic damping. Moreover, studies by Aguilar Sandoval et al.[56] and Pottier et al.[57] show that the frequency shift in such devices may result from the temperature dependence of elastic and other physical constants, especially when the temperature increase is significant. Accordingly, our first study focuses on the global linear response at 293 K and other absolute temperatures that do not rise above 100 K. We adjusted the 100 Hz frequency shift for temperatures up to 380 K. For the piezoelectric mode, the simulations were performed at 293 K as there was no significant temperature increase. Therefore, we used the classical thermo-piezoelectric finite element model with physical constants at different absolute temperatures. The latter combines the physics of piezoelectricity and heat transfer to predict the coupled behavior of materials under thermal and mechanical loading, typically using the finite element method. This model is essential for the development and analysis of devices where both thermal and piezoelectric effects play a role. The linear thermo-piezoelectric constitutive equations can be derived from the free thermo-piezoelectric energy potential[58] or by applying the Hamiltonian principle.[50–53] The linear thermo-piezoelectric system of constitutive equations can be obtained by using the notation in Table V. In these equations, a comma followed by a suffix denotes the material derivatives and a colon (:) denotes differentiation with respect to time.

$$\begin{cases} \sigma_{ij} = C_{ijkl}\,\varepsilon_{kl} - e_{kij}\,E_k - \beta_{ij}\,\theta \\ D_i = e_{ikl}\,\varepsilon_{kl} + d_{ik}\,E_k + \pi_i\,\theta \\ \rho\eta = \beta_{ij}\,\varepsilon_{ij} + \pi_k\,E_k + \rho c\,\theta \end{cases} \tag{6}$$

Then we use the classical equation of motion, the Gauss equation, and Fourier's law, which are given below.

$$\begin{cases} \rho\,\ddot{u}_i = \sigma_{ij,j} + f_i^{\Omega} \\ D_{i,i} = \rho_e = 0 \\ T_0\,\rho\dot{\eta} = -q_{i,i} + Q^{\Omega} \end{cases} \tag{7}$$

with the following classical relations:

$$\begin{cases} \varepsilon_{ij} = \frac{1}{2}(u_{i,j} + u_{j,i}) \\ E_i = -\phi_{,i} \\ q_i = -\kappa_{ij}\,\theta_{,j} \end{cases} \tag{8}$$

We derived the full coupling variational weak forms of the linear thermo-piezoelectric problem. Finally, we implemented these weak forms in FreeFem++[59] as a finite element solver both for eigenvalue and harmonic problems. The eigenvalue analysis was performed using the Lanczos method. The finite element analysis was conducted using the Galerkin method and the previous system of constitutive equations yields to the matrix/vector form below, labeled [.] for matrices and {.} for vectors.

$$\begin{cases} \{\sigma\} = [C]\{\varepsilon\} - [e]^{\mathsf{T}}\{E\} - \{\beta\}\theta \\ \{D\} = [e]\{\varepsilon\} + [d]\{E\} + \{\pi\}\theta \\ \quad \rho\eta = \{\beta\}^{\mathsf{T}}\{\varepsilon\} + \{\pi\}^{\mathsf{T}}\{E\} + \rho c\,\theta \end{cases} \tag{9}$$

Previously cited references[50–53,58] described the complete process calculations from weak forms to the global matrix system. The 3D linear thermo-piezoelectric model finally allowed us to determine the fundamental frequency mode for the different HTPC lengths with a relative error below 1%. We then focused the finite element model on the 306-µm-long U-shaped cantilever. Since it is assumed that AlN and platinum are isotropic for the considered physical constants, the modeling of this geometry is very simple. Moreover, since the length is a critical parameter for the eigenvalue analysis, we focus on the developed length of the prestressed cantilever. For simplicity, the HTPC was modeled by a circular profile so that the length of 306 µm corresponds to the arc.

In this study, the mesh consisted of about 10,900 nodes and 47,500 tetrahedral elements. To improve the efficiency of the finite element eigenvalue analysis, we ensured that the cantilever was modeled with ordered transfinite elements. In contrast, classical tetrahedral elements were used for the silicon volume part. To achieve better accuracy, quadratic Lagrangian interpolation was chosen, as linear interpolation may be less effective for first-mode calculations. The boundary conditions of zero displacement and temperature change were defined at the base of the silicon material. In accordance with the HTPC description, a ground potential was applied to the lower electrode and 1 V to the corresponding upper electrode. The elastic temperature dependence mainly affects AlN and platinum, since the main heating of the U-shaped cantilever is in the cantilever. The latter refers to how the elastic properties of a material, such as Young's modulus, shear modulus, and bulk modulus, vary with temperature. As the temperature increases, atomic vibrations become more pronounced, weakening the interatomic bonding forces and typically leading to a decrease in stiffness, which is reflected in a reduction of the material's Young's modulus. The elastic modulus often decreases either linearly or non-linearly with temperature, and the material's size may also change due to thermal expansion, affecting the internal stress state and thus influencing elasticity. Additionally, phase transitions in some materials can cause abrupt changes in their elastic properties. For instance, metals generally experience a gradual decrease in Young's modulus with rising temperature, while polymers may show more pronounced changes, especially near the glass transition temperature. Understanding this dependence is crucial in fields such as aerospace, electronics, and materials exposed to varying thermal conditions, as it ensures the material's mechanical integrity across a broad temperature range. According to,[60,61] the elastic physical properties were temperature interpolated with the starting point of Young's modulus of 186 GPa used in previous COMSOL modeling. The increased temperature in the silicon wafer was neglected

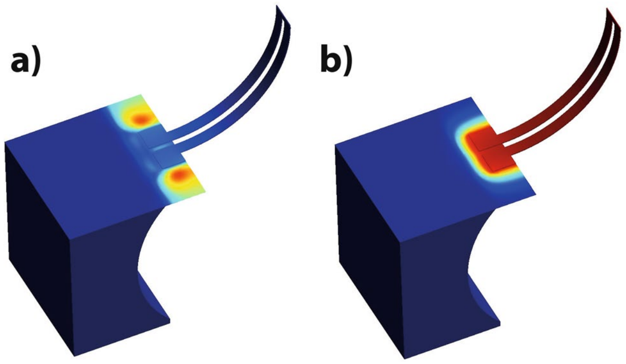

Fig. 8 Thermal flux of piezoelectric and thermo-piezoelectric modes (HSV linear color scale in arbitrary units): (a) thermal field for piezoelectric mode at 293 K, and (b) thermal field for thermal actuation mode at 380 K.

Table V Notations for the thermo-piezoelectric finite element model

σ_{ij}	Stress tensor	C_{ijkl}	Elasticity tensor
ε_{kl}	Strain tensor	e_{kij}	Piezoelectric tensor
E_k	Electric field vector	β_{ij}	Thermal isotropic stress tensor
θ	Temperature variation	D_i	Electric displacement vector
d_{ik}	Permittivity tensor	π_i	Pyroelectric vector
ρ	Mass density	η	Entropy density
c	Specific heat capacity	u_i	Displacement vector
f_i^{Ω}	Volume forces vector	ρ_e	Electric charge density
T_0	Reference temperature	q_i	Heat flux vector
Q^{Ω}	Volumetric heat source	ϕ	Electric potential
κ_{ij}	Thermal conductivity tensor		

as it is massive compared to the thin cantilever. The silicon wafer has a thickness of 500 ± 25μm, while the U-shaped cantilever has a total thickness of 1.22 μm. We can observe in Fig. 8 that the heating takes place in the electrodes and the AlN cantilever. We deduced from the finite element simulations that the thermal release mode acts as a volumetric heat source in the upper electrode due to the Joule heating as seen in Fig. 8a. Therefore, we observed the frequency shift experimentally and compared these results with a temperature of 380 K in the HTPC, as observed in Fig. 8b. In our experimental observations, the hybrid actuation mode induced a more pronounced frequency shift compared to other modes. Specifically, a frequency shift of 100 Hz corresponded to an approximate temperature increase of 90 K. Consequently, an experimental frequency shift of about 1.5 kHz indicated a significant temperature rise. Under these conditions, our linear finite element model became inadequate due to significant nonlinear heating phenomena. We hypothesized that both the top and bottom electrodes contributed to the heating of the AlN cantilever through the Joule heating effect, with the heating effect amplified when the AlN beam was sandwiched between the electrodes. Given the aspect ratio of our HTPC, the thermal convection and radiation losses were managed mainly by the bottom electrode in the thermal activation mode where only one electrode was active. However, in the hybrid thermo-piezoelectric mode, both electrodes heated the AlN beam, resulting in lower heat dissipation and thus higher temperatures. This increased temperature could significantly affect the performance and reliability of the device. Therefore, it was found that it is crucial to consider these thermal effects in the design and analysis of hybrid thermo-piezoelectric systems.

Although the focus of this study was on the dominant piezoelectric and thermal effects driving HTPCs, we acknowledge the potential contributions of surface effects and flexoelectricity, especially for small structures. Bending deformation of AlN cantilevers can produce significant strain gradients, leading to a flexoelectric polarized field that could either enhance or attenuate piezoelectric coupling depending on the gradient magnitude and direction.[62–64] Moreover, surface effects could influence the mechanical responses and performance of piezoelectric bimorph actuators, as demonstrated in recent studies.[65] Although these effects have not been explicitly considered in the current theoretical framework, their potential influence is recognized, especially for thinner films or nanoscale devices. Future modeling efforts will aim to integrate the contributions of strain gradient induced polarization fields and surface phenomena to provide a more comprehensive understanding of the behavior of HTPCs under hybrid actuation. These considerations will be especially relevant for applications requiring high sensitivity or where miniaturization leads to dominant nanoscale effects. This study, which focuses on larger cantilevers (length 300 μm), provides fundamental insights into hybrid actuation mechanisms. However, the inclusion of flexoelectric and surface effects in future work could lead to a more refined model and broader applicability of HTPCs, especially in high curvature or high strain gradient regions. The inclusion of these effects will enable deeper exploration of performance optimization and support the design of the next generation of piezoelectric and thermo-piezoelectric micro/nano-devices.

Further nonlinear analysis of the hybrid thermo-piezoelectric mode should be carried out in future work. Namely, we need to implement a nonlinear finite element model that takes into account the temperature dependence of the physical constants, the spatial dependence of the absolute temperature, the convective and radiative heat losses, and the dissipative Joule heating effect. This background before device design will be important for developing more complex devices tailored for targeted applications, such as harvesting energy from vibrations,[66] which is a very promising technology. Indeed, these vibrations produced in HTPCs in different electronic systems can be harvested. Thus, the heating combined with vibrational energy can be converted into electrical energy, which can be stored and efficiently used to power low-energy electronic devices, even in harsh environments.[5,67,68]

Conclusion

This study investigated the design and performance of hybrid thermo-piezoelectric cantilevers (HTPCs) for microactuation applications that combine piezoelectric and thermal actuation mechanisms. Through finite element simulations using COMSOL Multiphysics and FreeFem++, we investigated the dynamics of these cantilevers under different actuation modes and configurations. Key findings include the significant influence of material properties, such as Young's modulus of elasticity of AlN, on the resonant frequencies and displacement capabilities of the HTPCs. Experimental validations using a laser Doppler vibrometer confirmed the predicted behaviors and showed minimal frequency shifts under varying voltages in piezoelectric mode and significant shifts due to thermal effects. We highlighted challenges and future directions for nonlinear modeling to account for temperature-dependent material properties and heat dissipation effects. HTPCs show promising potential for applications such as vibration energy harvesting and low-power microdevices, as they efficiently utilize thermal and piezoelectric effects.

Acknowledgments The authors acknowledge the cleanroom and characterization laboratory staff at C2N, ESIEE, and FEMTO-ST technological facility. This work was partly supported by the French RENATECH network and its technological facility.

Author Contributions Conceptualization, E.H., B. C., F. L-D.; methodology, E.H., B.C, S.S., F.K.; writing-original draft preparation, B.C, S.S., F.K. and E.H.; formal analysis, validation, B.C, S.S., F.K., F. L-D., D.F., L.R. L.B. and E.H.; methodology, E.H., B.C, S.S., F.K. All authors have read and agreed to the published version of the manuscript.

Funding Open access funding provided by Université Paris-Saclay. This research received no external funding.

Data Availability Not applicable.

Material Availability Applicable.

Conflict of interest The authors declare that they have no conflict of interest.

Ethics Approval and Consent to Participate Not applicable.

Consent for Publication Not applicable.

References

1. S. Saravanan, J.W. Berenschot, G.J. Krijnen, M.C. Elwenspoek, Surface micromachining process for the integration of ALN piezoelectric microstructures, in *Annual Workshop on Semiconductor Advances for Future Electronics, SAFE 2004* (2004)
2. N. Smagin, M. Vanotti, M. Duquennoy, L. Rousseau, H. Alhousseini, V. Blondeau-Patissier, M. Ouaftouh, L. Valbin, and E. Herth, Electrical and optical characterization of saw sensors coated with parylene C and their analysis using the coupling-of-modes (COM) theory. *Sensors* 22(22), 8611 (2022).
3. T. Kovalevich, D. Belharet, L. Robert, G. Ulliac, M.-S. Kim, H.P. Herzig, T. Grosjean, and M.-P. Bernal, Bloch surface waves at the telecommunication wavelength with lithium niobate as the top layer for integrated optics. *J. Appl. Opt.* 58(7), 1757 (2019).
4. M.-A. Dubois and P. Muralt, Properties of aluminum nitride thin films for piezoelectric transducers and microwave filter applications. *J. Appl. Phys. Lett.* 74(20), 3032 (1999). https://doi.org/10.1063/1.124055.
5. E. Herth, D. Fall, J.-Y. Rauch, V. Mourtalier, and G. Guisbiers, Thermal annealing of AlN films for piezoelectric applications. *J. Mater. Sci.: Mater. Electron.* 31(6), 4473 (2020). https://doi.org/10.1007/s10854-020-02984-w.
6. V. Lacour, E. Herth, F. Lardet-Vieudrin, J.J. Dubowski, and T. Leblois, GaAs based on bulk acoustic wave sensor for biological molecules detection. *Procedia Eng.* 120, 721 (2015).
7. N. Smagin, L. Djoumi, E. Herth, M. Vanotti, D. Fall, V. Blondeau-Patissier, M. Duquennoy, and M. Ouaftouh, Fast time-domain laser Doppler vibrometry characterization of surface acoustic waves devices. *Sens. Actuators, A* 264, 96 (2017).
8. M. Baudoin, P. Brunet, O. Bou Matar, and E. Herth, Low power sessile droplets actuation via modulated surface acoustic waves. *J. Appl. Phys. Lett.* 100(15), 154102 (2012). https://doi.org/10.1063/1.3701725.
9. T. Baron, E. Lebrasseur, F. Bassignot, H. Wang, S. Ballandras, J. Fan, L. Catherinot, M. Chatras, P. Monfraix, and L. Estagerie, Wideband lithium niobate FBAR filters. *Int. J. Microw. Sci. Technol.* 31, 4473 (2013).
10. M. Link, M. Schreiter, J. Weber, R. Primig, D. Pitzer, and R. Gabl, Solidly mounted ZnO shear mode film bulk acoustic resonators for sensing applications in liquids. *IEEE Trans. Ultrason.* 53(2), 492 (2006).
11. X. Bian, H. Jin, X. Wang, S. Dong, G. Chen, J.K. Luo, M.J. Deen, and B. Qi, UV sensing using film bulk acoustic resonators based on Au/n-ZnO/piezoelectric-ZnO/Al structure. *Sci. Rep.* 5, 9123 (2015).
12. N.B. Moussa, M. Lajnef, N. Jebari, C. Villebasse, F. Bayle, J. Chaste, A. Madouri, R. Chtourou, and E. Herth, Synthesis of ZnO sol-gel thin-films CMOS-Compatible. *RSC Adv.* 11(37), 22723 (2021).
13. B.M. Nizar, M. Lajnef, J. Chaste, R. Chtourou, and E. Herth, Highly C-oriented (002) plane ZnO nanowires synthesis. *RSC Adv.* 13(22), 15077 (2023).
14. A. Benouhiba, D. Belharet, A. Bienaimé, V. Chalvet, M. Rakotondrabe, and C. Clévy, Development and characterization of thinned PZT bulk technology based actuators devoted to a 6-DOF micropositioning platform. *J. Microelectron. Eng.* 197, 53 (2018).
15. R. Herdier, M. Detalle, D. Jenkins, C. Soyer, and D. Remiens, Piezoelectric thin films for MEMS applications-a comparative study of PZT, 0.7PMN-0.3PT and 0.9PMN-0.1PT thin films grown on Si by R.F. magnetron sputtering. *Sens. Actuators, A* 148(1), 122 (2008).
16. D. Dezest, O. Thomas, F. Mathieu, L. Mazenq, C. Soyer, J. Costecalde, D. Remiens, J.F. Deü, and L. Nicu, Waferscale fabrication of self-actuated piezoelectric nanoelectromechanical resonators based on lead zirconate titanate (PZT). *J. Micromech. Microeng.* 25(3), 035002 (2015).
17. E. Herth, L. Valbin, F. Lardet-Vieudrin, and E. Algré, Modeling and detecting response of micromachining square and circular membranes transducers based on AlN thin film piezoelectric layer. *J. Microsyst. Technol.* 23(9), 3873 (2017). https://doi.org/10.1007/s00542-015-2727-9.
18. E. Herth, E. Algré, J.-Y. Rauch, J.-C. Gerbedoen, N. Defrance, and P. Delobelle, Modeling and characterization of piezoelectric beams based on an aluminum nitride thin-film layer. *Phys. Status Solidi (A)* 213(1), 114 (2016).
19. M. Feneberg, R.A.R. Leute, B. Neuschl, K. Thonke, and M. Bickermann, High-excitation and high-resolution photoluminescence spectra of bulk AlN. *J. Phys. Rev. B* 82(7), 075208 (2010). https://doi.org/10.1103/PhysRevB.82.075208.
20. J.Li, K.B. Nam, M.L. Nakarmi, J.Y. Lin, H.X. Jiang, P. Carrier, and S.-H. Wei, Band structure and fundamental optical transitions in wurtzite AlN. *J. Appl. Phys. Lett.* 83(25), 5163 (2003). https://doi.org/10.1063/1.1633965.
21. G.A. Slack, R.A. Tanzilli, R.O. Pohl, and J.W. Vandersande, The intrinsic thermal conductivity of AIN. *J. Phys. Chem. Solids* 48(7), 641 (1987).
22. N. Watanabe, T. Kimoto, and J. Suda, The temperature dependence of the refractive indices of GaN and AlN from room temperature up to 515 °C. *J. Appl. Phys.* 104(10), 106101 (2008). https://doi.org/10.1063/1.3021148.
23. P.T. Lin, H. Jung, L.C. Kimerling, A. Agarwal, and H.X. Tang, Low-loss aluminium nitride thin film for mid-infrared

microphotonics. *Laser Photonics Rev.* 8(2), L23 (2014). https://doi.org/10.1002/lpor.201300176.

24. Y. Taniyasu, M. Kasu, and T. Makimoto, An aluminium nitride light-emitting diode with a wavelength of 210 nanometres. *Nature* 441(7091), 325 (2006).
25. Y. Aono, S. Hata, J. Sakurai, R. Yamauchi, H. Tachikawa, and A. Shimokohbe, Basic research on combinatorial evaluation method for coefficient of thermal expansion. *MRS Online Proc. Libr. Arch.* 1024, 1 (2007).
26. D.H. Kim, Y.C. Park, and S. Park, Design and fabrication of twisting-type thermal actuation mechanism for micromirrors. *Sens. Actuators, A* 159(1), 79 (2010).
27. E. Pichonat-Gallois, V. Petrini, and M. de Labachelerie, Design and fabrication of thermal actuators used for a micro-optical bench: application to a tunable Fabry-Perot filter. *Sens. Actuators, A* 114(2), 260 (2004).
28. M. Rakotondrabe, and I.A. Ivan, Development and dynamic modeling of a new hybrid thermopiezoelectric microactuator. *IEEE Trans. Robot.* 26(6), 1077 (2010).
29. M. Rakotondrabe, I.A. Ivan, Development and force/position control of a new hybrid thermo-piezoelectric MicroGripper dedicated to micromanipulation tasks. *IEEE Trans. Autom. Sci. Eng.* 8(4), 824 (2011).
30. H. Pourrostami, H. Zohoor, and M.H. Kargarnovin, Development, modeling and deflection analysis of hybrid micro actuator with integrated thermal and piezoelectric actuation. *Meccanica* 48, 1081 (2013).
31. X.-J. Dong and G. Meng, Dynamic analysis of structures with piezoelectric actuators based on thermal analogy method. *Int. J. Adv. Manuf. Technol.* 27(9), 841 (2006). https://doi.org/10.1007/s00170-004-2290-5.
32. K. Schwarz, U. Rabe, S. Hirsekorn, and W. Arnold, Excitation of atomic force microscope cantilever vibrations by a Schottky barrier. *Appl. Phys. Lett.* 92(18), 183105 (2008). https://doi.org/10.1063/1.2911916.
33. I. Cimalla, C. Foerster, V. Cimalla, V. Lebedev, D. Cengher, and O. Ambacher, Wet chemical etching of AlN in KOH solution. *Phys. Status Solidi C* 3(6), 1767 (2006). https://doi.org/10.1002/pssc.200565206.
34. D. Chen, J. Wang, D. Xu, and Y. Zhang, The influence of the AlN film texture on the wet chemical etching. *Microelectron. J.* 40(1), 15 (2009).
35. S.M. Tanner and V.V. Felmetsger, Microstructure and chemical wet etching characteristics of AlN films deposited by ac reactive magnetron sputtering. *J. Vacuum Sci. Technol. A* 28(1), 69 (2010). https://doi.org/10.1116/1.3268620.
36. E. Herth, M. Baranski, D. Berlharet, S. Edmond, D. Bouville, L.E. Calvet, and C. Gorecki, Fast ultra-deep silicon cavities: toward isotropically etched spherical silicon molds using an ICP-DRIE. *J. Vacuum Sci. Technol. B* 37(2), 021206 (2019). https://doi.org/10.1116/1.5081503.
37. E. Herth, D. Belharet, S. Edmond, D. Bouville, L. Robert, and F. Lardet-Vieudrun, Screening of spherical moulds manufactured isotropically in plasma etching conditions. *Contrib. Plasma Phys.* 61(7), e202100023 (2021). https://doi.org/10.1002/ctpp.202100023.
38. C. Geuzaine and J.-F. Remacle, GMSH: a 3-D finite element mesh generator with built-in pre- and post-processing facilities. *Int. J. Numer. Methods Eng.* 79(11), 1309 (2009). https://doi.org/10.1002/nme.2579.
39. E. Herth, F. Lardet-Vieudrin, L. Valbin, and E. Algré, Detecting response of square and circular SI, AlN, AL membranes transducers by laser vibrometry Doppler and impedancemeter, in *Symposium on Design, Test. Integration and Packaging of MEMS/MOEMS (DTIP)* (2015), pp. 1–5
40. E. Herth, F. Lardet-Vieudrin, L. Valbin, and G. Lissorgues, Mechanical behavior of t-shaped a1n membrane based on thin film elongation acoustic resonator, in *Symposium on Design, Test. Integration and Packaging of MEMS/MOEMS (DTIP)* (2016), pp. 1–4
41. E. Herth, F. Lardet-Vieudrin, F. Deux, L. Valbin, E. Algré, J. Schell, and H. Steger, Detection of out-of-plane and in-plane (XYZ) motions of piezoelectric microcantilever by 3D-laser doppler vibrometry, in *Symposium on Design, Test. Integration and Packaging of MEMS/MOEMS (DTIP)* (2016), pp. 1–4
42. J.O. Dennis, W.A. Talha, and N.H.B. Hamid, Characterization and modeling of 3-D vibration modes of a micromachined U-shaped cantilever, in *Symposium on Design. Test, Integration Packaging of MEMS/MOEMS* (2009), pp. 8–13
43. A. Boisen, S. Dohn, S.S. Keller, S. Schmid, and M. Tenje, Micromechanical sensors. *Rep. Progr. Phys.* 74(3), 036101 (2011).
44. S. Adhikari, Inertial mass sensing with low q-factor vibrating microcantilevers. *J. Appl. Phys.* 122(14), 144304 (2017). https://doi.org/10.1063/1.4993678.
45. A. Andrei, K. Krupa, M. Jozwik, P. Delobelle, L. Hirsinger, C. Gorecki, L. Nieradko, and C. Meunier, AlN as an actuation material for MEMS applications: the case of AlN driven multilayered cantilevers. *Sens. Actuators, A* 141(2), 565 (2008).
46. S. Timoshenko, *JOSA* 11(3), 233 (1925).
47. J.B. Wachtman, W.E. Tefft, D.G. Lam, and C.S. Apstein, Exponential temperature dependence of Young's modulus for several oxides. *J. Phys. Rev.* 122(6), 1754 (1961). https://doi.org/10.1103/PhysRev.122.1754.
48. N. Chen, P. Yan, and J. Ouyang, An improved model analysis approach for hybrid thermo-piezoelectric micro actuator with thermo-piezoelectric coupling. *Measurement* 136, 517 (2019).
49. B. Sviličić, G.S. Wood, E. Mastropaolo, and R. Cheung, Thermal- and piezo-tunable flexural-mode resonator with piezoelectric actuation and sensing. *J. Microelectromech. Syst.* 26(3), 609 (2017).
50. W. Nowacki, Some general theorems of thermopiezoelectricity. *J. Therm. Stress.* 1(2), 171 (1978). https://doi.org/10.1080/01495737808926940.
51. M. Aouadi, Generalized thermoelastic-piezoelectric problem by hybrid Laplace transform-finite element method. *Int. J. Comput. Methods Eng. Sci. Mech.* 8(3), 137 (2007). https://doi.org/10.1080/15502280701252404.
52. X. Tian, J. Zhang, Y. Shen, and T.J. Lu, Finite element method for generalized piezothermoelastic problems. *Int. J. Solids Struct.* 44(18), 6330 (2007).
53. A. Kumar and S. Kapuria, Wave packet enriched finite element for accurate modelling of thermoelectroelastic wave propagation in functionally graded solids. *Appl. Math. Comput.* 477, 128796 (2024).
54. S. Guha and A.K. Singh, Frequency shifts and thermoelastic damping in different types of nano-/micro-scale beams with sandiness and voids under three thermoelasticity theories. *J. Sound Vib.* 510, 116301 (2021).
55. S. Guha, A.K. Singh, and S. Singh, Thermoelastic damping and frequency shift of different micro-scale piezoelectro-magneto-thermoelastic beams. *Phys. Scr.* 99(1), 015203 (2023). https://doi.org/10.1088/1402-4896.
56. F.A. Aguilar Sandoval, M. Geitner, É. Bertin, and L. Bellon, Resonance frequency shift of strongly heated micro-cantilevers. *J. Appl. Phys.* 117(23), 234503 (2015).
57. B. Pottier, F. Aguilar Sandoval, M. Geitner, F. Esteban Melo, and L. Bellon, Silicon cantilevers locally heated from 300 K up to the melting point: temperature profile measurement from their resonances frequency shift. *J. Appl. Phys.* 129(18), 184503 (2021). https://doi.org/10.1063/5.0040733.

58. J.L. Pérez-Aparicio, R. Palma, and R.L. Taylor, Multiphysics and thermodynamic formulations for equilibrium and non-equilibrium interactions: non-linear finite elements applied to multi-coupled active materials. *Arch. Comput. Methods Eng.* 23(3), 535 (2016). https://doi.org/10.1007/s11831-015-9149-9.
59. F. Hecht, New development in freeFem++. *J. Numer. Math.* 20(3–4), 251 (2012).
60. A. Wang, S.-L. Shang, M. He, Y. Du, L. Chen, R. Zhang, D. Chen, B. Fan, F. Meng, and Z.-K. Liu, Temperature-dependent elastic stiffness constants of FCC-based metal nitrides from first-principles calculations. *J. Mater. Sci.* 49(1), 424 (2014). https://doi.org/10.1007/s10853-013-7721-y.
61. R.P. Singh, Temperature dependence of elastic constants and bulk modulus of metals. *Asian J. Adv. Basic Sci.* 2(1), 116 (2014).
62. L. Sun, L. Zhu, C. Zhang, W. Chen, and Z. Wang, Mechanical manipulation of silicon-based Schottky diodes via flexoelectricity. *Nano Energy* 83, 105855 (2021).
63. J. Wu, C. Wu, W. Zhang, C. Zhang, and W. Chen, Manipulation of bilayer MoS2-based MESFET with flexoelectric polarization field. *Nano Energy* 123, 109415 (2024).
64. J. Narvaez, F. Vasquez-Sancho, and G. Catalan, Enhanced flexoelectric-like response in oxide semiconductors. *Nature* 538(7624), 219 (2016). https://doi.org/10.1038/nature19761.
65. C. Zhang, C. Zhang, and W. Chen, Modeling of piezoelectric bimorph nano-actuators with surface effects. *J. Appl. Mech.* 80(6), 061015 (2013). https://doi.org/10.1115/1.4023693.
66. D. Diab, N. Smagin, F. Lefebvre, G. Nassar, S. Isber, F. El Omar, and A. Naja, Broadband vibrational energy harvesting with a spherical piezoelectric transducer devoted to underwater wireless sensor networks. *Acta Acust. United Acust.* 105(4), 616 (2019).
67. S. Saxena, R.K. Dwivedi, and V. Khare, Multi-piezoelectric materials based doubly clamped energy harvester. *J. Mater. Sci.: Mater. Electron.* 31(9), 6998 (2020). https://doi.org/10.1007/s10854-020-03266-1.
68. E. Lefeuvre, A. Badel, A. Brenes, S. Seok, M. Woytasik, and C.-S. Yoo, Analysis of piezoelectric energy harvesting system with tunable SECE interface. *Smart Mater. Struct.* 26(3), 035065 (2017).